Effect of local chain stiffness on oligomer crystallization from a melt

Pierre Kawak
Department of Chemical, Biological and Materials Engineering, University of South Florida, Tampa, Florida 33612, USA

Christopher Akiki and Douglas R. Tree*
Chemical Engineering Department, Brigham Young University, Provo, Utah 84602, USA

(Received 14 March 2024; accepted 9 July 2024; published 23 July 2024)

While the process by which a polymer crystal nucleates from the melt has been extensively studied via molecular simulation, differences in polymer models and simulated crystallization conditions have led to seemingly contradictory results. We make steps to resolve this controversy by computing low-temperature phase diagrams of oligomer melts using Wang-Landau Monte Carlo simulations. Two qualitatively different crystallization mechanisms are possible depending on the local bending stiffness potential. Polymers with a discrete bending potential crystallize via a single-step mechanism, whereas polymers with a continuous bending potential can crystallize via a two-step mechanism that includes an intermediate nematic phase. Other model differences can be quantitatively accounted for using an effective volume fraction and a temperature scaled by the bending stiffness. These results suggest that at least two universality classes of nucleation exist for melts and that local chain stiffness is a key determining factor in the mechanism of nucleation.

DOI: 10.1103/PhysRevMaterials.8.075606

I. INTRODUCTION

Given the scale of production and the ubiquity of semicrystalline polymers, polymer crystallization remains one of the most important, and most challenging, fundamental problems in polymer science [1]. Despite decades of study, the mechanism by which a crystal first nucleates in a polymer melt remains controversial [2]. The conventional theory, classical nucleation theory (CNT), treats the transition between polymer melt and a crystal nucleus as a single-step transition [3]. However, for the most widely studied case of polyethylene (PE) crystallization, there are numerous experimental observations of mesoscale precursors prior to crystal formation [4–12]. Subsequently, as shown in Fig. 1, a number of researchers have proposed multistep theories of polymer crystal nucleation [13–16]. For example, Olmsted *et al.* proposed that a metastable liquid–liquid phase separation intervenes to assist nucleation [13], and Strobl *et al.* [14] and Milner [15] separately proposed that PE crystallizes via a nematically aligned intermediate.

The multistep theories of nucleation by Olmsted, Strobl, Milner, and others rely on the existence of specific (but different) low-temperature thermodynamic behavior as a necessary (but not sufficient) condition. Consequently, although kinetics are critical to the process of polymer crystallization and the resulting microstructure, *a study of the thermodynamics of polymer crystallization is necessary for evaluating the plausibility of these theories.* Additionally, a better understanding of polymer crystallization thermodynamics will provide context for understanding kinetic effects. Finally, all theories of polymer nucleation predict that free-energy barriers dominate system dynamics, and we recently showed that equilibrium methods can be used to calculate free-energy landscapes (FELs), providing values of free-energy barriers and identifying metastable states [17]. Knowledge of the phase diagram is a necessary prerequisite for determining FELs. We argue, therefore, that the low-T equilibrium behavior of long-chain molecules continues to require attention, despite the importance of kinetics.

In this paper, we use Wang-Landau Monte Carlo (WLMC) simulations [18,19] to construct low-T equilibrium phase diagrams of a homopolymer melt for several different models of polymers. Unfortunately, even equilibrium simulations of polymer crystallization are numerically costly, so we are presently limited to relatively small systems composed of short chains. We are particularly interested in the existence and location of intermediate phases, such as a nematic phase, that may assist the nucleation process. Here, we focus specifically on how the "virtual chemistry" (i.e., the molecular potentials) of the polymer affects the phase diagram. We find that, at least for these relatively small systems, the bending stiffness of the chain plays a critical role in determining the equilibrium phase behavior.

A. The current state of molecular simulations of polymer crystal nucleation

Molecular simulations appear ideally suited to directly address the mechanism of primary nucleation for polymers, but the simulation literature contains significant disagreements. For example, several research groups modelled crystallization of a united-atom model of PE and found evidence that supports the single-step transition described by CNT, including

*Contact author: tree.doug@byu.edu

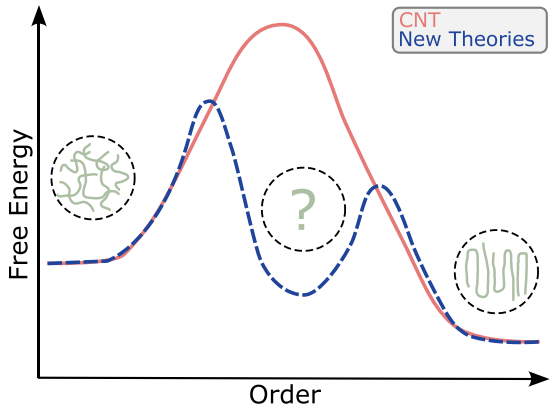

FIG. 1. Schematic of free-energy landscape separating a metastable melt from the crystal resulting from CNT, a single-step mechanism, and newer theories postulating two-step phase transitions.

a cylindrical critical nucleus and a lack of nematic ordering before crystallization [20–25]. On the other hand, other researchers have observed nematic ordering in simulations of *n*-alkanes and PE [26,27], as well as a noncylindrically shaped nucleus, providing evidence for a two-step transition [3,26–31]. Simulations of flow-induced crystallization of PE also provide evidence that chain orientation plays a role in nucleation [32–34].

There are at least two significant issues to consider when seeking to resolve these apparent discrepancies in the literature. First, one must consider the role that kinetics play in the crystallization process, and more specifically, in simulations. Polymer crystallization is a notoriously nonequilibrium process, although exactly which effects are due to thermodynamics and which are due to kinetics remain a subject of vigorous debate [24,25,29,30].

Because kinetics are so important, most simulation studies use nonequilibrium molecular dynamics (NEMD) to study nucleation. In NEMD, a polymer melt is equilibrated above the melting point T_m, and then instantaneously quenched to a temperature $T_c < T_m$, where it crystallizes. Since homogeneous nucleation is a rare event in a dense melt [35], a large degree of supercooling $S = (T_m - T_c)/T_m$ is used [36] to reduce the nucleation time to the order of nanoseconds [20–22,37–46]. Consequently, nucleation rates in NEMD are highly accelerated relative to experiments [47], and the rapid crystallization rates in simulations are believed to significantly impact the nucleation mechanism [23–26]. Thus, one reason for the apparent contradictions could be different kinetic protocols, leading to qualitatively different crystallization behavior.

A second possible reason for the discrepancy could be the differences between the molecular potentials. A numerical polymer model can be thought of as its *virtual monomer chemistry* [48], and thus the relation between molecular potentials and crystallization behavior is related to the question of "universality" in polymer crystallization. The principle of universality in polymer physics applies when chain-level degrees of freedom dominate the physical behavior independent of monomer chemistry [49], and this concept is widely invoked for more coarse-grained phenomena such as block copolymer self-assembly and entanglement dynamics. Its usefulness for polymer crystallization is more complicated because there are some phenomena, such as crystal structure, that are monomer dependent and thus clearly not universal, but others, such as the formation of folded lamellae, appear to be common to nearly all polymer chemistries.

The simulations of PE cited above employ various (all-atom or united-atom) force fields including Paul-Yoon-Smith (PYS) [50], OPLS [51,52], flexible Williams (FW) [53], Shinoda-DeVane-Klein (SDK) [54,55], TraPPE [56], and Siepmann-Karaboni-Smit (SKS) [57]. All of these models are parameterized for the well-studied system of monodisperse linear *n*-alkanes, and at first blush, it seems surprising that the equilibrium crystallization behavior of these models could be qualitatively different. Nevertheless, there are important differences in the degree of coarse graining between some of these models, and coarse graining can indeed produce important effects on phase behavior [26,39,58]. Therefore, it is possible that some of these different numerical model "chemistries" could belong to different universality classes of crystallization.

B. Our approach

In the present paper, we use equilibrium simulation methods to investigate the crystallization phase behavior of several model polymers. *Our objective is to catalog which monomer "chemistries" lead to a given "universality class" of equilibrium crystallization behavior.* Equilibrium methods eliminate the need for a kinetic protocol that has made it difficult to interpret and compare simulations of polymer crystal nucleation in the literature. By avoiding one of the key sources of variation between simulations in the literature, we are free to focus on examining how differences in molecular potentials lead to different crystallization thermodynamics.

Note an important caveat when connecting the results that follow with the nucleation theories discussed at the outset. The *equilibrium universality class* (phase behavior and FEL) is not equivalent to the *dynamic universality class* for nucleation; the latter involves dissipative processes that may, for example, lead to the kinetically preferred formation of a metastable state. However, we hypothesize that it is a necessary condition for two systems to reside within the same equilibrium universality class in order to be within the same dynamic universality class. Stated less abstractly, a phase diagram must be compatible with a given nucleation theory (one-step or two-step), but the existence of a compatible phase diagram is not positive proof of a nucleation mechanism.

Unfortunately, even neglecting kinetics, simulating polymer crystallization is numerically expensive, and it is difficult and costly to calculate phase diagrams of dense melts containing long chains with accurate molecular potentials. Indeed, these limitations widely impede progress in the field. Therefore, we resort here to two simplifying assumptions in order to make progress.

First, we use short oligomers. Shorter chains significantly reduce simulation costs, which are substantial due to low temperatures, large nucleation barriers, and extended chains. In particular, a crystalline state consisting of fully extended

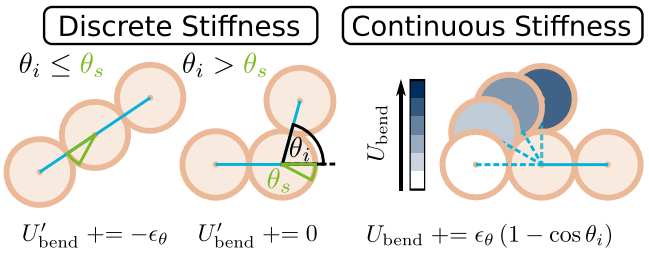

FIG. 2. Schematic of the two families of bending stiffness: discrete and continuous.

chains requires a relatively large simulation box (compared to simulations of a melt) to avoid unphysical self-interactions. Using short chains therefore limits the required size of the box, helping to reduce finite-size effects. We obtain valuable results despite the relatively short chains, and we anticipate future progress in our abilities to reach larger system sizes as we improve our methods.

Second, we use relatively simple molecular potentials. The use of simple polymer models may also appear unwise, because, as discussed, the details of crystallization necessarily depend on atomic-level structure. However, we use simple models because they are less expensive to simulate, they facilitate comparison with prior studies [17,59–64] and possible generalization.

The rest of the paper proceeds as follows. We detail our methods in Sec. II, with Sec. II A explaining the polymer models and parameters, and Sec. II B detailing the protocol for constructing phase diagrams. The main results are contained in Sec. III, beginning with the identification of the low-T phases and phase transition temperatures in Sec. III A. We then present the phase diagrams of the various models and the effect of bending stiffness on phase behavior in Sec. III B. After ascertaining the impact of the bending stiffness, we explore the effects of excluded volume on phase behavior in Sec. III C. We then offer brief concluding remarks and a perspective for future research in Sec. IV.

II. METHODS

Our WLMC simulations consist of a melt of $N_c = 125$ chains that contain $N_b = 10$ beads per chain in a periodic box of volume V. They generate representative melt configurations and a density of states $\Omega(U)$ as a function of potential energy U. $\Omega(U)$ is postprocessed to compute a heat capacity $C_V(T)$ and temperature profiles of various crystalline and nematic order parameters (OPs) [17,65–67]. We performed WLMC simulations at different volume fractions,

$$\phi = \frac{\pi a^3 N_c N_b}{6V}, \tag{1}$$

where a is the bead size, in the range $\phi \in [0.2, 0.5]$ to obtain phase diagrams as a function of both T and ϕ.

We focus on two different families of polymer models, shown in Fig. 2, based on the way local chain stiffness is calculated: (i) a "discrete stiffness" family employing a discontinuous bending potential that has recently been used in several studies of oligomer crystallization [17,59,67], and (ii) a "continuous stiffness" family of models (equivalent to a Kratky–Porod or wormlike chain [68]) consisting of polymers whose stiffness comes from a harmonic bending potential between adjacent bonds. The model of a polymer chain must also include a bonding potential U_{stretch} and a nonbonded (excluded volume) pair potential U_{pair}. We examine multiple models for U_{stretch} and U_{pair} within each of the two families. For U_{stretch}, we study rigid-rod and harmonic bonding potentials with a bond length scale l_0, whereas for U_{pair}, we employ hard-bead and soft repulsive (Weeks-Chandler-Anderson, WCA) nonbonded potentials characterized by the parameter σ. There are no attractive interactions in the models discussed here. Several authors have provided evidence that attractive interactions are of secondary importance for the qualitative phase behavior [37–40,59,60,69], and we leave a deeper investigation of this issue to future work.

The following sections detail the methods we used to collect, analyze, and interpret our results. Section II A describes the coarse-grained polymer models and their potentials in greater detail. Then, Sec. II B details the protocol for determining phase diagrams, including a description of the order parameters that we use. Further methodological details are found within the Supplemental Material (SM) [70] (see also Refs. [18,19,59,64,71–90] therein).

A. Polymer models and parameterization

We use a coarse-grained model that has been estimated to be roughly equivalent to about four CH_2 monomers of polyethylene for one coarse-grained bead [52]. While this unfortunately sacrifices atomic-level accuracy, these models allow one to capture important polymer physics including connectivity, excluded volume, and chain stiffness. The latter is especially important for our present purposes as we seek to understand what is *universal* about the crystallization behavior among several different polymer models.

A polymer model is defined by the total potential energy,

$$U_{\text{tot}} = U_{\text{bend}} + U_{\text{stretch}} + U_{\text{pair}}, \tag{2}$$

where U_{bend} is the bond angle bending energy, U_{stretch} is the bond length stretching energy, and U_{pair} is the nonbonded (pairwise) potential energy. In this paper, we study eight different polymer potential variations: two for each of the potentials (bending, stretching, and nonbonded) in Eq. (2).

The family of polymer models is defined by the bending potential, which accounts for polymer chain stiffness. The continuous stiffness (i.e., wormlike) potential is a harmonic bending potential between adjacent bonds,

$$U_{\text{bend}} = \sum_{i=1}^{N_c(N_b-1)} u_{\text{cont}}(\theta_i), \tag{3}$$

$$u_{\text{cont}}(\theta_i) = \epsilon_\theta(1-\cos\theta_i), \tag{4}$$

where

$$\boldsymbol{l}_i = \boldsymbol{r}_{i+1} - \boldsymbol{r}_i \tag{5}$$

is the bond vector between bead i and its neighbor along the backbone of the chain, $l_i = |\boldsymbol{l}_i|$ is the bond length,

$$\theta_i = \frac{\boldsymbol{l}_i \cdot \boldsymbol{l}_{i-1}}{l_i l_{i-1}} \tag{6}$$

is the bond angle, and ϵ_θ is the bending elasticity. The discrete stiffness (i.e., square-well) potential is given by

$$U_{\text{bend}} = \sum_{i=1}^{N_c(N_b-1)} u_{\text{disc}}(\theta_i), \tag{7}$$

$$u_{\text{disc}}(\theta_i) = \begin{cases} -\epsilon_\theta & \theta_i \leqslant \theta_s \\ 0 & \theta_i > \theta_s \end{cases}, \tag{8}$$

where $\theta_s = \cos^{-1}(0.9)$ is a critical upper bound on bond angles that are favored. Both types of potentials incentivize chains to adopt extended conformations.

Each model family (continuous or discrete stiffness) has four different possible combinations of stretching ("rod-like" and "spring") and nonbonded ("hard-sphere" and "soft-sphere") potentials. The rod-like stretching potential is given by

$$U_{\text{stretch}} = \sum_{i=1}^{N_c(N_b-1)} u_{\text{rod}}(l_i), \tag{9}$$

$$u_{\text{rod}}(l_i) = \begin{cases} \infty & l_i \neq l_0 \\ 0 & l_i = l_0 \end{cases}, \tag{10}$$

where l_0 is the equilibrium bond length. Equation (10) only allows constant bond lengths, which we set to be the size of the nominal bead diameter a. The spring stretching potential is harmonic and is given by

$$U_{\text{stretch}} = \sum_{i=1}^{N_c(N_b-1)} u_{\text{spring}}(l_i), \tag{11}$$

$$u_{\text{spring}}(l_i) = \frac{\epsilon_l}{2}(l_i - l_0)^2, \tag{12}$$

where $\epsilon_l = 600 k_B T/a^2$ is the bond spring constant and $l_0 = a$. Polymers that use Eq. (12) have bonds that fluctuate around l_0 to a degree that depends on the strength of ϵ_l.

The hard-sphere nonbonded potential accounts for purely repulsive excluded volume interactions and is given by

$$U_{\text{pair}} = \sum_{i=1}^{N_c N_b} \sum_{j=1}^{N_n(i)} u_{\text{hard}}(r_{ij}), \tag{13}$$

$$u_{\text{hard}}(r_{ij}) = \begin{cases} \infty & r_{ij} < \sigma \\ 0 & r_{ij} \geqslant \sigma \end{cases}, \tag{14}$$

where $r_{ij} = |\boldsymbol{r}_j - \boldsymbol{r}_i|$ is the distance between beads i and j, $N_n(i)$ are the number of neighbors of bead i with a nonzero pairwise potential, and σ is the hard-bead diameter, which is set equal to a. The soft-sphere nonbonded potential is the purely repulisve Weeks-Chandler-Anderson (WCA) potential given by

$$U_{\text{pair}} = \sum_{i=1}^{N_c N_b} \sum_{j=1}^{N_n(i)} u_{\text{WCA}}(r_{ij}), \tag{15}$$

$$u_{\text{WCA}}(r_{ij}) = \begin{cases} 4\epsilon_{ij}\left[\left(\frac{\sigma}{r_{ij}}\right)^{12} - \left(\frac{\sigma}{r_{ij}}\right)^{6}\right] + \epsilon_{ij} & r_{ij} < 2^{1/6}\sigma \\ 0 & r_{ij} \geqslant 2^{1/6}\sigma \end{cases}, \tag{16}$$

where ϵ_{ij} and σ are the WCA pair potential energy and length scale, respectively. The value of σ in the WCA potential is set to $2^{-1/6}a$ so that the effective bead diameter is commensurate with the equilibrium bond length l_0, ensuring that crystallization is possible [64,87] (details available within the SM [70]). Notably, neither of these nonbonded potentials include attractive interactions. We neglect them here for simplicity, but we note that several studies suggest that their effect is a simple shift of the temperature dependence of the phase diagram [37–40,59,60,69]. A summary of the parameters for each potential are given in Table I.

TABLE I. Summary of parameters for the various potentials used in the study.

	Bending potential θ_s	
Discrete (D)	$\cos^{-1}(0.9)$	
Continuous (C)	N/A	
	Stretching potential ϵ_l	l_0
Rod (R)	N/A	a
Spring (S)	$600\epsilon_\theta/a^2$	a
	Nonbonded potential ϵ_{ij}	σ
Hard (H)	N/A	a
WCA (W)	ϵ_θ	$2^{-1/6}a$

Dimensional analysis reveals that there are six dimensionless groups that could control the phase behavior. At minimum, this includes the dimensionless volume fraction ϕ, the bond length–bead diameter aspect ratio $l_0^* = l_0/a$, and the reduced temperature $T_r = k_B T/\epsilon_\theta$. In addition, if the model uses a WCA nonbonded potential (instead of a hard-sphere potential) then there is a dimensionless bending stiffness scale $\epsilon_\theta^* = \epsilon_\theta/\epsilon_{ij}$, if the model includes a harmonic stretching potential (instead of the rigid-rod potential) then there is a dimensionless spring stiffness $\epsilon_l^* = \epsilon_l/(\epsilon_{ij}a^2)$, and if the model includes a discrete stiffness bending potential (instead of the continuous potential) then $\cos\theta_s$ is also a group.

Where appropriate, we set $\cos\theta_s = 0.9$, $l^* = 1$, and $\epsilon_l^* = 600$, and did not explore other values of these groups. We chose $\cos\theta_s = 0.9$ to enable comparisons with Refs. [59] and [17] and to facilitate nematic alignment. If $l^* \neq 1$, the bonds are incommensurate with the bead diameter and crystallization is inhibited [64,87]. A large value of ϵ_l^* gives stiff springs; soft springs are physically unrealistic for studying crystallization and our preliminary testing suggested that phase behavior was relatively insensitive to this parameter.

The more interesting dimensionless groups are ϕ, ϵ_θ^*, and T_r, and we produce phase diagrams in ϕ–T_r space with volume fractions $\phi \in [0.2 - 0.5]$, $T_r \in [0, 0.5]$, and $\epsilon_\theta^* \in \{0.1, 1, 10\}$. The high-$\phi$ simulations are quite dense; for comparison, the volume fractions of random and maximum close-packed configurations of hard spheres are 0.64 and $\pi/(3\sqrt{2}) \approx 0.7405$, respectively [91].

Finally, because there are numerous combinations of potentials, it is useful to define a systematic naming scheme for the models. We define our scheme based on the choice of potentials in the polymer model, following the order: bending potential (discrete or continuous), stretching potential (rods or springs), and nonbonded potential (hard or WCA). For

TABLE II. Naming scheme for polymer models.

Systematic name	Shorthand
DRH (Discrete, Rod, Hard)	Model A
DRW (Discrete, Rod, WCA)	
DSH (Discrete, Spring, Hard)	
DSW (Discrete, Spring, WCA)	
CRH (Continuous, Rod, Hard)	Model B
CRW (Continuous, Rod, WCA)	
CSH (Continuous, Spring, Hard)	
CSW (Continuous, Spring, WCA)	Model C

example, a model with a discrete bending potential Eq. (7), rod-like bonds Eq. (9), and a hard-sphere nonbonded potential Eq. (13) is labeled the DRH model. Because they are used frequently in this paper, the DRH model, the CRH model, and the CSW model are also labeled Models A, B, and C respectively for ease of reference. The naming scheme and shorthand names are summarized for clarity in Table II.

B. Procedure for constructing phase diagrams

The entropy obtained from a WLMC simulation can be used to compute heat capacity and order parameter profiles as a function of temperature, enabling the identification of phases and phase transitions. By sweeping volume fraction in different simulations, one can construct phase diagrams in the $\phi - T_r$ plane. This section presents a brief overview of the procedure for the creation of these phase diagrams, including details of the order parameters used to identify the phases. Note that we have also previously identified these phases in a system nearly identical to Model A using real-space images and two-dimensional structure factors [17,67].

Specifically, we observe three phases in this system: a disordered melt phase (I), a nematic phase (N), and a crystal phase (C). We use two order parameters, f_{cryst} and P_2, to quantify crystalline and nematic order in these phases. f_{cryst} represents the fraction of crystalline beads based on the well-known Steinhardt order parameter [17,65,66], and P_2 is the second Legendre polynomial, a measure of nematic order [17].

We use heat capacity and order parameter curves to locate the relevant phase transition temperatures: isotropic–nematic (IN), isotropic–crystal (IC) and nematic–crystal (NC). The constant-volume heat capacity is given by

$$\langle C_V(T)\rangle = \frac{\langle U^2(T)\rangle - \langle U(T)\rangle^2}{k_B T^2}, \tag{17}$$

where the moments of U are calculated using

$$\langle U^n(T)\rangle = \frac{\sum_i U_i^n \exp(\ln \Omega_i - U_i/k_B T)}{\sum_i \exp(\ln \Omega_i - U_i/k_B T)}, \tag{18}$$

and U_i and $\Omega_i = \Omega(U_i)$ are discrete states of the energy and density of states obtained from the WLMC simulation. It is also useful to define a dimensionless heat capacity,

$$\tilde{C}_V = \frac{\langle C_V\rangle}{k_B N_c (N_b - 2)}. \tag{19}$$

At a phase transition temperature T_m, $\tilde{C}_V(T_m)$ exhibits a large narrow peak.

Order parameter "melting curves" can be obtained using

$$\langle M(T)\rangle = \frac{\sum_i \langle M_i\rangle \exp(\ln \Omega_i - U_i/k_B T)}{\sum_i \exp(\ln \Omega_i - U_i/k_B T)}, \tag{20}$$

where M is an order parameter such as P_2 or f_{cryst} and $M_i = M(U_i)$. The order parameter curves $\langle M\rangle$ exhibit discontinuities at a phase transition temperature.

The parameter P_2 characterizes the average local nematic alignment of the polymer chain contours. The chain orientation is determined by computing the angle between the bond vectors of a polymer chain with those of its neighbors. More precisely, each of the N_c chains contains $N_b - 1$ bond vectors,

$$\boldsymbol{l}_i = \boldsymbol{r}_i - \boldsymbol{r}_{i-1}, \tag{21}$$

and a local order parameter for each bond vector is given by

$$p_2(i) = \tfrac{3}{2}\langle \cos^2\theta_{ij}\rangle_{\text{neigh}} - \tfrac{1}{2}, \tag{22}$$

where θ_{ij} is the angle between bond vectors $\boldsymbol{l}_i$ and $\boldsymbol{l}_j$, and the average $\langle\rangle_{\text{neigh}}$ is over all j neighbors (regardless of which chain) that lie within a distance of 1.3σ from $\boldsymbol{r}_i$. The global order parameter is calculated as an average over all bond vectors in the system using

$$P_2 = \langle p_2(i)\rangle. \tag{23}$$

P_2 varies from zero when the system is isotropic, to one when all bond vectors are perfectly aligned along a single direction.

The parameter f_{cryst} is the fraction of monomers in the system that are crystalline. Following Reinhardt *et al.* [66], we define a monomer to be crystalline if it resides in a cluster with a minimum number of neighbors with solid-like ordering. Solid ordering is determined by the pairwise local order parameter

$$d_l(i,j) = \boldsymbol{q}_l(i)\cdot \boldsymbol{q}_l^*(j), \tag{24}$$

between beads i and j that are within a pairwise distance of 1.3σ. The vectors

$$\boldsymbol{q}_l(i) = [q_{l,m}(i)]^T, \tag{25}$$

in Eq. (24) have $2l+1$ components that are the Steinhardt order parameters of bead i [65],

$$q_{l,m}(i) = \langle Y_{l,m}(\boldsymbol{r}_{ij})\rangle_{\text{neigh}}, \tag{26}$$

with $m \in [-l, l]$. In the above, $\boldsymbol{q}_l^*$ is the complex conjugate of $\boldsymbol{q}_l$, $Y_{l,m}$ is the spherical harmonic function of degree l and order m, $\boldsymbol{r}_{ij} = \boldsymbol{r}_j - \boldsymbol{r}_i$ is the vector between bead i and its neighbor j, and $\langle\rangle_{\text{neigh}}$ is again the average over all neighbors within a distance of 1.3σ of $\boldsymbol{r}_i$. The symmetries of the hexagonal crystals formed by these molecules are well distinguished by sixth-order ($l = 6$) Steinhardt parameters, and so we use q_6.

Using these definitions, we can more precisely define a monomer to be crystalline when there are at least n_c neighbors within a distance of 1.3σ where $d_6(i,j) > d_c$. In this paper, we set the critical solid ordering parameter to be $d_c = 0.6$ and the minimum number of neighbors to be $n_c = 6$. Mathematically, the number of crystalline neighbors of bead i can be

expressed as

$$n_{\text{cryst}}(i) = \sum_{j=1}^{N_n(i)} H(d_6(i,j) - d_c), \tag{27}$$

where $H(x)$ is the Heaviside function

$$H(x) = \begin{cases} 1 & x > 0 \\ 0 & x \leqslant 0, \end{cases} \tag{28}$$

and $N_n(i)$ is the number of neighbors of bead i within a radius of $r_{ij} < 1.3a$. Finally, the total fraction of crystalline monomers f_{cryst} is determined via

$$f_{\text{cryst}} = \langle H(n_{\text{cryst}}(i) - n_c) \rangle. \tag{29}$$

As is the case with P_2, the value of f_{cryst} is zero when the system has no crystalline order and approaches one when the chains fully crystallize.

III. RESULTS AND DISCUSSION

A. Order parameter thermal profiles for Model A and Model B

Our goal is to construct phase diagrams in the $\phi - T_r$ plane for various models to probe the universality of phase behavior. In this section, we provide details of the calculations that are necessary to determine phase diagrams for Models A and B. As outlined in Sec. II B, WLMC simulations permit the direct calculation of Ω as a function of energy at a fixed volume fraction ϕ. One can then use Ω and simulation configurations to compute the order parameter as a function of temperature. The values and discontinuities in the order parameter thermal profiles enable one to identify the phases and the location of the phase transitions.

Figure 3 shows Ω for a representative system of Model A at $\phi = 0.463$. The relevant energy range

$$U \in [-N_c(N_b - 2)\epsilon_\theta, 0] \tag{30}$$

is subdivided into 32 overlapping WLMC windows (with eight replicates for each window). To accelerate convergence, we used a replica-exchange scheme where configurations are exchanged between windows and an entropy-exchange method where global histograms and entropies are aggregated from replicates. After all windows converge, shown in Fig. 3(a), the areas of overlap between windows are used to stitch together a global Ω, shown in Fig. 3(b). This latter step is necessary because Ω is only known to within an arbitrary constant. The inset of Fig. 3(b) shows the least-squares stitching procedure for the last two windows ($R^2 = 0.998$).

In addition to Ω, configurations generated from the last WLMC iteration ($n = 27$) can be used to compute the nematic and crystal order parameters. Figure 3(c) shows curves of P_2 and f_{cryst} obtained from WLMC (averaged over the eight replicates) as a function of U. At high U, both order parameters are small indicating that the high-energy state is a disordered melt. By contrast, both order parameters rise significantly above zero at the ground state ($U = -1000\epsilon_\theta$), indicating the occurrence of a crystal phase.

We desire phase diagrams in the $\phi - T_r$ plane, so we use the equations in Sec. II B to transform the data to be a function of T rather than U. Accordingly, Fig. 4 shows thermal profiles of the nematic order parameter P_2, the fraction of crystalline beads f_{cryst}, and the dimensionless heat capacity $\tilde{C}_V$ for Model A and Model B at both low and high values of the volume fraction ϕ.

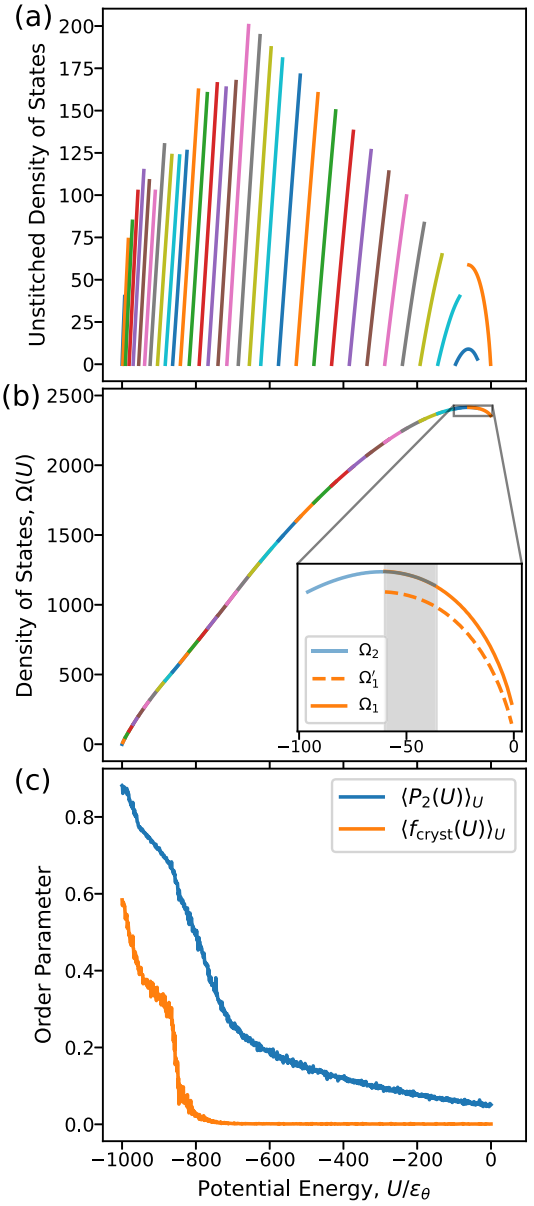

FIG. 3. Direct result of WLMC simulations for Model A at $\phi = 0.463$. (a) Density of states Ω for 32 overlapping windows, averaged over eight replicates, vs potential energy U. (b) The "stitched" global Ω with inset showing the stitching protocol for the rightmost pair of windows. Ω' in the inset corresponds to the value before stitching. (c) Average order parameters P_2 and f_{cryst} as a function of U. The apparent level of noise is a consequence of the small bin size of U.

Figure 4(a) shows thermal profiles for the order parameters and heat capacity for Model A at the relatively low-volume fraction $\phi = 0.407$. At high T_r the system has small values of nematic and crystalline order, characteristic of an isotropic melt. At low T_r, P_2 rises significantly but f_{cryst} does not, indicating a transition to a phase with orientational (but not crystalline) order. This isotropic (I) to nematic (N) transition happens at $T_r = T_{IN} \approx 0.246$, where P_2 sharply increases and

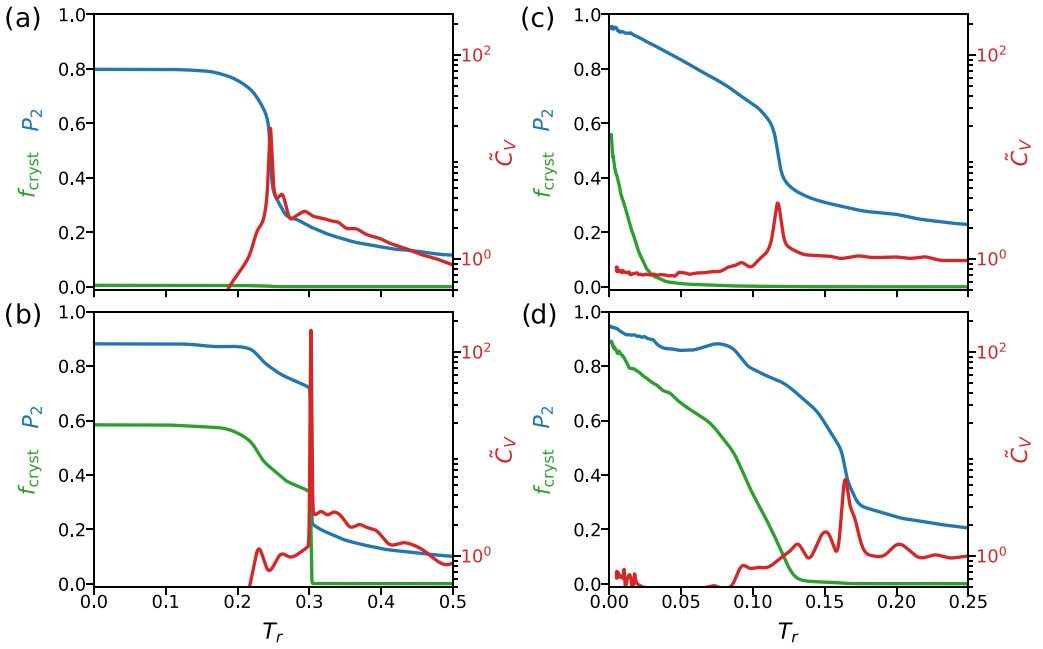

FIG. 4. Thermal profiles of P_2 in blue, f_{cryst} in green, and $\tilde{C}_V$ in red. (a) WLMC simulation of Model A at a low-volume fraction ($\phi = 0.407$) showing a discontinuity at $T_r = 0.246$. (b) WLMC simulation of Model A at a high volume fraction ($\phi = 0.463$) showing a discontinuity at $T_r = 0.302$. (c) WLMC simulation of Model B at a low-volume fraction ($\phi = 0.407$) showing two discontinuities at $T_r = 0.025$ and $T_r = 0.117$. (d) WLMC simulation of Model B at a high-volume fraction ($\phi = 0.463$) showing two discontinuities at $T_r = 0.131$ and $T_r = 0.164$.

the heat capacity $\tilde{C}_V$ shows a distinct peak. The step discontinuity in the order parameter and divergence in the heat capacity at T_{IN} (tempered by finite-size effects) are classical indicators of a first-order phase transition.

Figure 4(b) shows corresponding thermal profiles for P_2, f_{cryst}, and $\tilde{C}_V$ for Model A at a larger volume fraction $\phi = 0.463$. Once again, P_2 and f_{cryst} are small at high T_r—evidence that the system is an isotropic melt. At low T_r, both P_2 and f_{cryst} show a pronounced increase, indicating the simultaneous development of both orientational and crystalline order. In other words, there is an isotropic (I) to crystalline (C) transition that happens at $T_r = T_{IC} \approx 0.302$, and again, the appearance of step discontinuities and a narrow peak in the heat capacity at the same temperature provide evidence that this is a first-order transition. Notably, at this higher volume fraction, the IC transition temperature is at a larger T_r than the IN transition, showing the impact of system density on the transition temperature as well as the nature of the transition.

The behavior of Model B differs qualitatively from that of Model A at both low- and high-volume fraction. Figure 4(c) shows P_2, f_{cryst}, and $\tilde{C}_V$ for Model B at the relatively low-volume fraction of $\phi = 0.407$. As before, the values of P_2 and f_{cryst} are small at large T_r indicating an isotropic melt. Unlike the previous results, in this case there are *two* phase transitions. At $T_r = T_{IN} \approx 0.117$ there is a jump in the nematic order parameter P_2 and a peak in $\tilde{C}_V$, indicative of an isotropic–nematic transition. In addition, at $T_r = T_{NC} \approx 0.025$ there is a rapid rise in the crystalline order parameter f_{cryst}, marking a transition from a nematic to a crystalline phase.

Notably, $\tilde{C}_V$ shows no distinguishable peak at this transition. We explain the lack of a second peak to a low "signal-to-noise" ratio, i.e., this transition has a small heat of fusion (see the SM [70] for curves of the internal energy) making the peak small, and there is statistical sampling error in the heat capacity (a second-order derivative of Ω) that makes the peak indistinguishable from noise. Physically, we reason that the heat of fusion for the crystallization transition is small, because the chains are already nematically aligned, and positional ordering is a relatively small collective movement from aligned chains. Regardless, the order parameter profiles make it clear that crystallization in this system requires a transition from an isotropic melt to a nematic phase, and a transition from a nematic to a crystal phase.

The evidence for two transitions is further reinforced by simulations at higher volume fraction. Figure 4(d) shows plots of the thermal profiles of P_2, f_{cryst}, and $\tilde{C}_V$ for Model B at $\phi = 0.463$. Here the results are qualitatively similar to the lower-density case, with an IN transition at $T_{IN} \approx 0.164$ and an NC transition at $T_{NC} \approx 0.131$. Again in this case, because of a small heat of fusion, one cannot distinguish the peak in the heat capacity for the crystallization transition from statistical sampling error, which give rise to spurious fluctuations in $\tilde{C}_V$ that are on the order of k_B per bead.

From the above, we conclude that there are three equilibrium phases in Model A and Model B: an isotropic melt (I), a nematic phase (N), and a crystal phase (C). Additionally, we find evidence that isochoric crystallization in Model A proceeds via a single step, but takes place in two steps in Model B. The data for Model A agrees with our previous study that also included images of real-space configurations, 2D structure factors, and other order parameters [17].

B. Comparison of the phase behavior of Model A and Model B

In this section, we explore in greater detail the surprising result that Model A has a single-step melt to crystalline

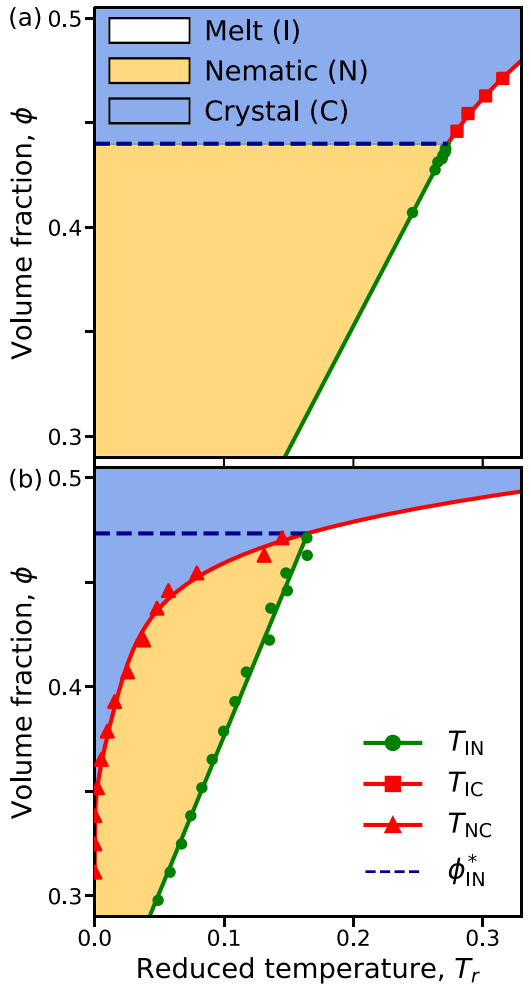

FIG. 5. Phase diagrams for (a) Model A and (b) Model B in the $\phi-T_r$ plane containing crystalline (C), nematic (N), and isotropic melt (I) phases. Solid curves are least-square fits to the data provided as a guide to the eye.

transition, whereas Model B has a two-step transition with an intermediate nematic phase. Recall that the only difference between these models is the form of the bending potential: Model A has a discontinuous square-well potential, and Model B has a continuous wormlike potential. We first compile the results from numerous WLMC simulations of Model A and Model B at different volume fractions into phase diagrams in the $\phi-T_r$ plane in Figure 5. The order parameter profiles for both models at all values of ϕ that are used to create these phase diagrams are provided in the SM [70].

The phase diagram for Model A is shown in Fig. 5(a), and it contains two types of transitions along isochores. At low ϕ, there is a transition T'_{IN} from an isotropic melt to a nematic phase. At high ϕ, there is a transition T'_{IC} from an isotropic to a crystalline phase. Separating these two transitions, there is an isochoric critical volume fraction $\phi'^*_{IN} = 0.440$.

The phase diagram for Model B is shown in Fig. 5(b), and it displays qualitatively different behavior. For nearly all of the volume fractions we computed, there is an isotropic to nematic transition T_{IN} along an isochore, and a nematic to crystal transition that follows at $T_{NC} < T_{IN}$. At very low ϕ, the NC transition occurs at or very close to $T_r = 0$ or it disappears entirely. As we discuss below, we suspect that this behavior is due to the temperature-dependent stiffness of the chains at low T_r. At high ϕ, the IN and NC curves appear to converge, and we speculate that there is a single-step IC transition T_{IC} beyond a critical point $(T^*_{IN}, \phi^*_{IN}) \approx (0.164, 0.473)$. Unfortunately, we were unable to directly observe a single-step IC transition in Model B due to large computational costs for very dense systems.

It is useful to compare both of these models to a system of freely jointed chains (FJC) of hard spheres, which crystallizes at a critical volume fraction of $\phi^* \approx 0.57$ independent of temperature [61,92]. We hypothesize that the presence of temperature-dependent chain stiffness in the present models promotes alignment that reduces the volume fraction where crystallization can occur compared to the FJC.

The difference between the phase diagrams for the two models is relevant for the debate in the literature on the mechanism of polymer crystal nucleation. The crystallization transition for Model A when $\phi > \phi'^*_{IN}$ is a single-step transition consistent with CNT. By contrast, the crystallization transition for Model B when $\phi < \phi^*_{IN}$ is a two-step transition with a nematic intermediate, consistent with the theories of Strobl *et al.* [14] and Milner [15]. The change in equilibrium behavior will also significantly impact the free-energy barriers and the relative free energy of metastable intermediates, the latter of which has been shown to be important in flow-induced crystallization [27]. Computing such barriers requires a complete temperature-dependent free-energy surface [17], which we leave for future investigation.

It remains to understand *why* there is such a dramatic qualitative difference in the phase behavior of the two models. Because the only difference is the bending potential, we reason that chain stiffness must be a key factor. To better understand how chain stiffness differs between the two models, we computed the temperature dependence of the persistence length l_p for both types of chains. The persistence length is defined as the length scale that characterizes the decorrelation of segments along the chain backbone and is a measure of chain stiffness [81],

$$\langle \cos\theta(s) \rangle = \exp(-s l_0/l_p) \tag{31}$$

where $\theta(s)$ is the angle between two bonds along the chain separated by s bonds. To eliminate excluded volume and density effects, we calculated l_p using "phantom chain" (i.e., models neglecting nonbonded interactions) NVT-ensemble Monte Carlo (MC) simulations. Further details of these calculations are given within the SM [70].

In addition, as both models are types of freely rotating chains, it is possible to compute closed form expressions for the persistence length of both models as a function of temperature. The persistence length of a freely rotating chain is given by [81]

$$\frac{l_p}{l_0} = \frac{1}{2}\left[\frac{1+\langle\cos\theta\rangle}{1-\langle\cos\theta\rangle}\right]. \tag{32}$$

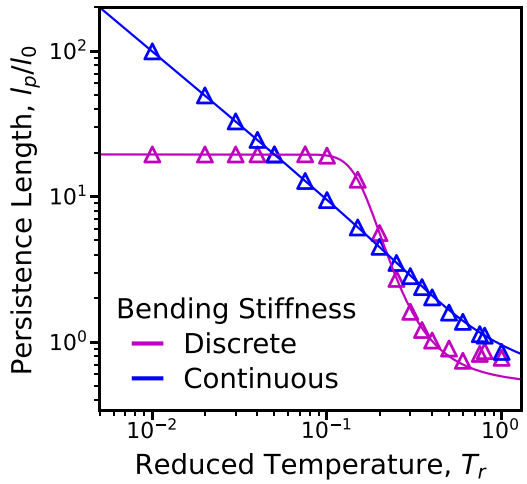

FIG. 6. Dimensionless persistence length l_p/l_0 vs reduced temperature $T_r = k_B T/\epsilon_\theta$ for phantom Model A (magenta) and phantom Model B (blue). For both models, lines are theoretical predictions (detailed in the SM [70]). The standard errors of data points are smaller than the size of the symbols.

For phantom Model A, the ensemble-averaged bond angle is given by

$$\langle \cos\theta \rangle = \frac{19}{20}\frac{\exp(1/T_r) - 1}{\exp(1/T_r) + 19}. \tag{33}$$

For phantom Model B, the average bond angle is given by

$$\langle \cos\theta \rangle = 1 - T_r - \frac{2}{1 - \exp(2/T_r)}. \tag{34}$$

Further details on the derivation of the relationship between the ensemble-averaged angle $\langle \cos\theta \rangle$ and temperature are available within the SM [70].

Figure 6 shows the dimensionless persistence length l_p/l_0 for phantom Model A and phantom model B versus the reduced temperature T_r alongside the theoretical expressions defined by Eqs. (32), (33), and (34). The data for the phantom chains agrees very well with the theoretical results. Intuitively, both models have a smaller l_p (indicating more flexible chains) at higher temperatures when thermal fluctuations are strong and a larger l_p (indicating stiffer chains) at lower temperatures when thermal fluctuations are weak. Additionally, both models become flexible as $T_r \to \infty$, approaching $l_p/l_0 = 0.5$ (the value for a freely jointed chain). Finally, we show in the SM [70] that data for phantom simulations with additional models (DSH, CSH) collapse to the same curves, indicating that the reduced temperature that has been normalized by the bending elasticity is the proper dimensionless parameter.

The differences in the persistence length curves between the models is more interesting. For Model A, the stiffness sharply increases around $T_r \approx 0.25$, and the persistence length converges to $l_p/l_0 = 19.5$ as $T_r \to 0$. By contrast, the chains in phantom Model B smoothly proceed from flexible to stiff and the persistence length diverges as $l_p \sim T_r^{-1}$ as $T_r \to 0$. Upon reflection, both behaviors are consistent with their respective bending potentials. The discontinuous stiffness in Model A has a finite reward per bond for remaining below θ_s, meaning increasingly low temperatures cannot induce further stiffening. On the other hand, the harmonic penalty for wormlike chains in Model B penalizes even minute deviations of bond angles from 180°, and this penalty increasingly dominates as T_r approaches 0.

Because the persistence length of the chains in Model B diverges and those in Model A do not, the most drastic difference between the models is at low T_r, precisely where crystallization occurs. We hypothesize that this difference in persistence length at low T_r is the cause of the differences in phase behavior, and therefore accounts for the one-step or two-step crystallization transition. In order for entropy to favor chain crystallization, the chain must either be (i) very stiff locally to prefer a lattice to conformational fluctuations (stiffness-driven crystallization) or (ii) it must be in a very dense environment to prefer the relative freedom of a lattice to liquid-like packing (density-driven crystallization). Chains in Model A align nematically as temperature decreases, but because l_p reaches a plateau, they apparently cannot become stiff enough to crystallize via mechanism (i). Thus, Model A must be above a critical density in order to crystallize, limiting them to a one-step crystallization transition at constant ϕ. By contrast, the chains in Model B have no such plateau, so a stiffness-driven crystallization is possible as temperature decreases even for moderate densities. Thus, Model B can exhibit an isochoric two-step crystallization transition.

C. Effect of excluded volume on the phase behavior of Model C

While useful for Monte Carlo studies, models with hard sphere repulsion and rigid bonds are rarely useful in molecular dynamics and are not compatible with simulations in a constant pressure ensemble. As such, in this section we investigate a model with a continuous bending potential, spring-like bonds, and nonbonded interactions modeled by a WCA potential (i.e., the CSW model or Model C). The softness of nonbonded interactions are also important for the debate on polyethyelene crystallization, because models with different levels of coarse graining are largely distinguished by their nonbonded interaction parameters. Accordingly, we investigate here if the relative strength of excluded volume interactions significantly alter the phase behavior [93,94].

The addition of spring-like bonds and soft-sphere repulsive interactions introduces new degrees of freedom to the dimensional analysis. The spring bonding potential Eq. (12) contains a length scale l_0 and an energy scale ϵ_l, and the WCA nonbonded potential Eq. (16) contains an energy scale ϵ_{ij}. As discussed in Sec. II A, l_0 is constrained to be equal to the bead diameter σ in order to ensure crystallization is possible. Additionally, very flexible bonds are only appropriate for capturing the "entropic spring" behavior of highly coarse-grained models, rather than the more detailed models we examine here that are appropriate for studying crystallization. As such, we are restricted to the case where $\epsilon_l \gg 1 k_B T/a^2$. Our preliminary tests with this parameter did not result in meaningful effects on low-temperature phase behavior.

By contrast, the strength of nonbonded interactions are very impactful for crystallization. We define a dimensionless parameter $\epsilon_\theta^* = \epsilon_\theta/\epsilon_{ij}$ as the ratio of the bending modulus to the excluded volume parameter. When $\epsilon_\theta^* \gg 1$, bending dominates over excluded volume interactions, and when

$\epsilon_\theta^* \ll 1$, the excluded volume interactions dominate over bending.

Figure 7 shows a phase diagram for Model C with $\epsilon_\theta^* \in \{0.1, 1, 10\}$ alongside the data for Model B from above. The thermal profiles for Model C used to create this diagram are given within the SM [70]. Similar to Model B, the phase diagram for Model C contains a IN transition at higher T_r and a NC transition at lower T_r along an isochore. While the phase diagram for Model C appears qualitatively similar to the behavior of Model B, there are apparent quantitative differences in the $\phi - T_r$ plane based on the relative strength of the excluded volume interactions ϵ_θ^*.

The isotropic to nematic (IN) transition line for Model C with $\epsilon_\theta^* \in \{0.1, 1, 10\}$ and for Model B is shown in Fig. 7(a). The line for hard bead interactions (Model B) appears to be the limiting behavior, and the IN line shifts to the left as excluded volume interactions weaken. In other words, for an equal value of ϕ, chains with softer nonbonded interactions order at a lower T_{IN}.

The nematic to crystallization transition line (NC) from the same simulations is shown in Fig. 7(b). Similarly, the hard bead interactions are to the right of all of the soft bead curves, with the NC line shifting to the left as the nonbonded interactions soften.

Apparently, for both types of transitions, softness reduces the drive to order. Given that both alignment and crystallization are driven by entropy, softer excluded volume interactions mean the effective bead size is smaller, giving the system relatively more degrees of freedom for individual bead motion. Finally, recall that T_r is normalized by the bending modulus, so the effect of bending is scaled out.

The importance of excluded volume reinforces the notion that the system volume fraction is of primary importance. However, the volume fraction ϕ defined in Eq. (1) does not account for the bead overlap that is permitted when using the softer WCA potential. As such, we compute an effective hard sphere diameter [71]

$$a_{\text{eff}} = \int_0^\infty (1 - e^{-U_{\text{pair}}(r_{ij})/k_B T}) dr_{ij}, \tag{35}$$

and use it to define an effective volume fraction

$$\phi_{\text{eff}}(T) = \frac{\pi a_{\text{eff}}^3 N_c N_b}{6V}. \tag{36}$$

Figure 7(c) shows the phase diagram for Model C using the newly defined ϕ_{eff}. Remarkably, both the IN and NC curves for all values of ϵ_θ^* collapse to the hard sphere data from Model B. From this, we infer that the dimensionless parameters ϕ_{eff} and T_r are sufficient to explain the phase behavior, and that Model C exhibits the same qualitative and quantitative phase behavior as Model B when properly scaled.

IV. CONCLUSIONS

We have shown that the crystallization behavior of simple polymer models critically depends on the character of its local stiffness. Using an equilibrium approach based on WLMC simulations, we simulated two families of relatively simple

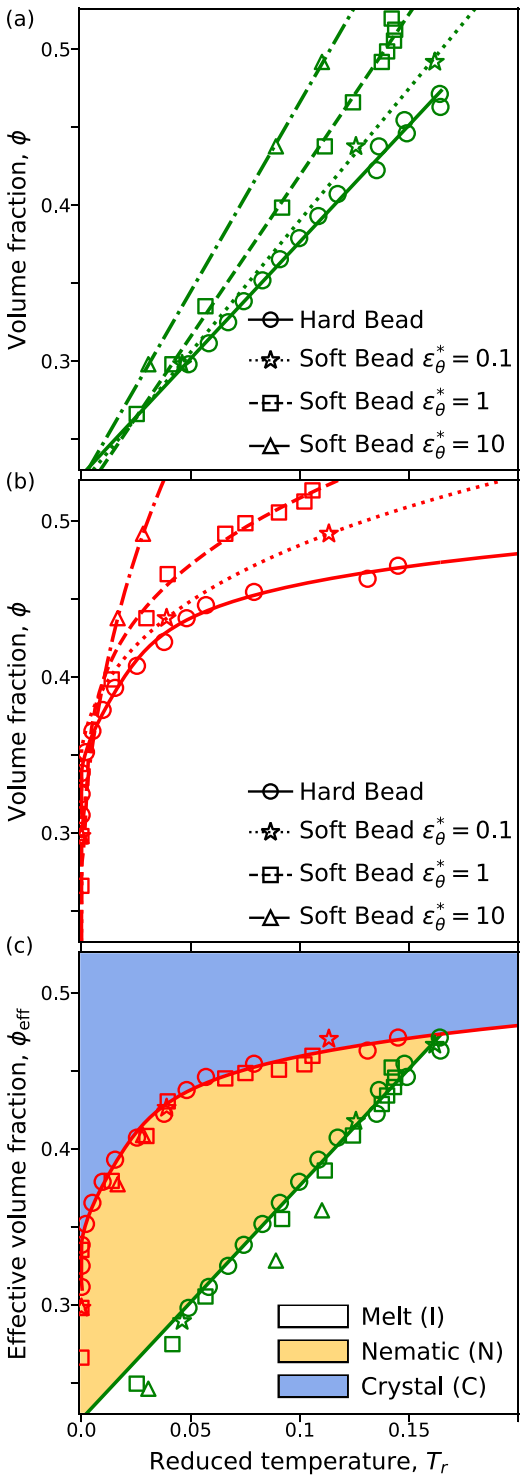

FIG. 7. Phase diagram for Model C (soft bead) where the parameter characterizing excluded volume interactions (ϵ_θ^*) varies over two orders of magnitude. Data for Model B (hard bead) is also shown for comparison. (a) The IN transition line in the $\phi - T_r$ plane for various values of ϵ_θ^*. Curves are drawn on the data to guide the eye. (b) The NC transition line in the $\phi - T_r$ plane for various values of ϵ_θ^*. Curves are drawn on the data to guide the eye. (c) All data in a rescaled phase diagram in the $\phi_{\text{eff}} - T_r$ plane. Lines and shading are unchanged from Fig. 5(b) above.

polymer models: polymers with a discontinuous local bending potential (Model A) and those with continuous local bending potential (Models B and C). Polymers in Model A exhibit only a one-step isochoric crystallization transition due to excluded volume interactions. By contrast, polymers in Models B and C can show a two-step isochoric crystallization transition that is mediated by nematic ordering. Importantly, the persistence length behavior of the chain is only a function of the reduced temperature, and its low temperature trend predicts the crystallization behavior.

Comparing simulations of hard beads (Model B) and purely repulsive soft beads (Model C) reveals that the strength of the excluded volume interactions also plays an important role in the crystallization behavior. Remarkably, these interactions are fully accounted for using an effective hard sphere diameter. Thus, the type of bending potential appears to determine the "universality class" of crystallization phase behavior for these models.

The hypothesis that local polymer stiffness controls the mechanism of polymer crystallization mechanism is intriguing but it has yet to be tested with chemistry-specific models or experimental data. Certainly, an immediate area of interest are models that include attraction and models with stiffness created by torsional degrees of freedom rather than bending. Notably, the role of attractive interactions has already generated attention, with recent research suggesting that attraction "shifts" phase boundaries but does not qualitatively change behavior [37–40,59,60,69].

Additionally, more study is needed related to the effects of a finite simulation box and chain length. Studies on finite-size scaling of first-order phase transitions [95–97] and our own preliminary data (see the SM [70]) suggest that the precise values of the transition temperatures (but not the relative location) may depend on the box size, but additional data is needed to perform a more careful study. The effects of polymer chain length are also very interesting and potentially have implications for the origin of folded-chain crystals [37,38,98]. Studies of both effects will require methodological refinements to be able to access larger simulation domains.

Regardless, the approach and results demonstrated here have the potential to reframe the ongoing debate about primary nucleation in polymer crystallization. For example, one can imagine reframing simulation parameters of existing models in terms of dimensionless groups with respect to universal phase diagrams. Doing so could help researchers rigorously compare their models and to better understand the effects of thermodynamics versus kinetics in determining the crystal nucleation mechanism.

ACKNOWLEDGMENTS

The authors thank the donors of the American Chemical Society Petroleum Research Fund (PRF Grant No. 59244-DNI6) and the BYU Board of Trustees for support of this research. Additionally, the authors acknowledge computational resources from the Office of Research Computing at Brigham Young University.

[1] T. P. Lodge, Celebrating 50 years of macromolecules, Macromolecules **50**, 9525 (2017).

[2] B. Lotz, T. Miyoshi, and S. Z. Cheng, *50th Anniversary perspective:* Polymer crystals and crystallization: Personal journeys in a challenging research field, Macromolecules **50**, 5995 (2017).

[3] S. Auer and D. Kashchiev, Two-step crystal nucleation kinetics: Solution of the master equation, J. Cryst. Growth **580**, 126469 (2022).

[4] G. Kanig, Application of the short-time staining for the electron microscopic investigation of the crystallization of polyethylene, Colloid Polym. Sci. **261**, 373 (1983).

[5] G. Kanig, Further electron microscope observations on polyethylene III. Smectic intermediate state during melting and crystallization, Colloid Polym. Sci. **269**, 1118 (1991).

[6] S. Rastogi, M. Hikosaka, H. Kawabata, and A. Keller, Role of mobile phases in the crystallization of polyethylene. Part 1. Metastability and lateral growth, Macromolecules **24**, 6384 (1991).

[7] E. B. Sirota, H. E. King, D. M. Singer, and H. H. Shao, Rotator phases of the normal alkanes: An x-ray scattering study, J. Chem. Phys. **98**, 5809 (1993).

[8] M. Imai, K. Mori, T. Mizukami, K. Kaji, and T. Kanaya, Structural formation of poly (ethylene terephthalate) during the induction period of crystallization: 1. Ordered structure appearing before crystal nucleation, Polymer **33**, 4451 (1992).

[9] G. Hauser, J. Schmidtke, and G. Strobl, The role of co-units in polymer crystallization and melting: New insights from studies on syndiotactic poly(propene-co-octene), Macromolecules **31**, 6250 (1998).

[10] N. J. Terrill, P. A. Fairclough, E. Towns-Andrews, B. U. Komanschek, R. J. Young, and A. J. Ryan, Density fluctuations: The nucleation event in isotactic polypropylene crystallization, Polymer **39**, 2381 (1998).

[11] G. Matsuba, K. Kaji, K. Nishida, T. Kanaya, and M. Imai, Conformational change and orientation fluctuations prior to the crystallization of syndiotactic polystyrene, Macromolecules **32**, 8932 (1999).

[12] Z.-G. Wang, B. S. Hsiao, E. B. Sirota, and S. Srinivas, A simultaneous small- and wide-angle x-ray scattering study of the early stages of melt crystallization in polyethylene, Polymer **41**, 8825 (2000).

[13] P. D. Olmsted, W. C. K. Poon, T. C. B. McLeish, N. J. Terrill, and A. J. Ryan, Spinodal-assisted crystallization in polymer melts, Phys. Rev. Lett. **81**, 373 (1998).

[14] G. Strobl, A thermodynamic multiphase scheme treating polymer crystallization and melting, Eur. Phys. J. E **18**, 295 (2005).

[15] S. T. Milner, Polymer crystal-melt interfaces and nucleation in polyethylene, Soft Matter **7**, 2909 (2011).

[16] M. Muthukumar, Communication: Theory of melt-memory in polymer crystallization, J. Chem. Phys. **145**, 031105 (2016).

[17] P. Kawak, D. S. Banks, and D. R. Tree, Semiflexible oligomers crystallize via a cooperative phase transition, J. Chem. Phys. **155**, 214902 (2021).

[18] F. Wang and D. P. Landau, Efficient, multiple-range random walk algorithm to calculate the density of states, Phys. Rev. Lett. **86**, 2050 (2001).
[19] M. P. Taylor, W. Paul, and K. Binder, Phase transitions of a single polymer chain: A Wang-Landau simulation study, J. Chem. Phys. **131**, 114907 (2009).
[20] P. Yi and G. C. Rutledge, Molecular simulation of crystal nucleation in *n*-octane melts, J. Chem. Phys. **131**, 134902 (2009).
[21] P. Yi and G. C. Rutledge, Molecular simulation of bundle-like crystal nucleation from *n*-eicosane melts, J. Chem. Phys. **135**, 024903 (2011).
[22] P. Yi, C. R. Locker, and G. C. Rutledge, Molecular dynamics simulation of homogeneous crystal nucleation in polyethylene, Macromolecules **46**, 4723 (2013).
[23] C. Luo and J.-U. Sommer, Disentanglement of linear polymer chains toward unentangled crystals, ACS Macro Lett. **2**, 31 (2013).
[24] C. Luo and J.-U. Sommer, Frozen topology: Entanglements control nucleation and crystallization in polymers, Phys. Rev. Lett. **112**, 195702 (2014).
[25] C. Luo and J.-U. Sommer, Role of thermal history and entanglement related thickness selection in polymer crystallization, ACS Macro Lett. **5**, 30 (2016).
[26] N. Wentzel and S. T. Milner, Crystal and rotator phases of *n*-alkanes: A molecular dynamics study, J. Chem. Phys. **132**, 044901 (2010).
[27] W. Zhang and R. G. Larson, A metastable nematic precursor accelerates polyethylene oligomer crystallization as determined by atomistic simulations and self-consistent field theory, J. Chem. Phys. **150**, 244903 (2019).
[28] K. W. Hall, T. W. Sirk, S. Percec, M. L. Klein, and W. Shinoda, Divining the shape of nascent polymer crystal nuclei, J. Chem. Phys. **151**, 144901 (2019).
[29] K. W. Hall, T. W. Sirk, S. Percec, M. L. Klein, and W. Shinoda, Monodisperse polymer melts crystallize via structurally polydisperse nanoscale clusters: Insights from polyethylene, Polymers **12**, 447 (2020).
[30] K. W. Hall, S. Percec, W. Shinoda, and M. L. Klein, Property decoupling across the embryonic nucleus-melt interface during polymer crystal nucleation, J. Phys. Chem. B **124**, 4793 (2020).
[31] Y. Gong, W. Zhang, and R. G. Larson, Interfacial oriented precursor to secondary nucleation of alkane oligomer crystals revealed by molecular dynamic simulations, Macromolecules **55**, 6311 (2022).
[32] D. A. Nicholson and G. C. Rutledge, An assessment of models for flow-enhanced nucleation in an *n*-alkane melt by molecular simulation, J. Rheol. **63**, 465 (2019).
[33] D. A. Nicholson and G. C. Rutledge, Flow-induced inhomogeneity and enhanced nucleation in a long alkane melt, Polymer **200**, 122605 (2020).
[34] W. Zhang and R. G. Larson, Effect of flow-induced nematic order on polyethylene crystal nucleation, Macromolecules **53**, 7650 (2020).
[35] C. Dellago and P. G. Bolhuis, Transition path sampling and other advanced simulation techniques for rare events, in *Advanced Computer Simulation Approaches for Soft Matter Sciences III*, Vol. 221, edited by C. Holm and K. Kremer (Springer, Berlin, 2009), pp. 167–233.
[36] Values of $S > 20\%$ are common.
[37] H. Meyer and F. Müller-Plathe, Formation of chain-folded structures in supercooled polymer melts, J. Chem. Phys. **115**, 7807 (2001).
[38] H. Meyer and F. Müller-Plathe, Formation of chain-folded structures in supercooled polymer melts examined by MD simulations, Macromolecules **35**, 1241 (2002).
[39] T. Vettorel and H. Meyer, Coarse graining of short polythylene chains for studying polymer crystallization, J. Chem. Theory Comput. **2**, 616 (2006).
[40] T. Vettorel, H. Meyer, J. Baschnagel, and M. Fuchs, Structural properties of crystallizable polymer melts: Intrachain and interchain correlation functions, Phys. Rev. E **75**, 041801 (2007).
[41] M. Anwar, F. Turci, and T. Schilling, Crystallization mechanism in melts of short *n*-alkane chains, J. Chem. Phys. **139**, 214904 (2013).
[42] M. Anwar, J. T. Berryman, and T. Schilling, Crystal nucleation mechanism in melts of short polymer chains under quiescent conditions and under shear flow, J. Chem. Phys. **141**, 124910 (2014).
[43] M. Anwar and T. Schilling, Crystallization of polyethylene: A molecular dynamics simulation study of the nucleation and growth mechanisms, Polymer **76**, 307 (2015).
[44] J. T. Berryman, M. Anwar, S. Dorosz, and T. Schilling, The early crystal nucleation process in hard spheres shows synchronised ordering and densification, J. Chem. Phys. **145**, 211901 (2016).
[45] L. Zou and W. Zhang, Molecular dynamics simulations of the effects of entanglement on polymer crystal nucleation, Macromolecules **55**, 4899 (2022).
[46] W. Zhang and L. Zou, Mismatch in nematic interactions leads to composition-dependent crystal nucleation in polymer blends, Macromolecules **56**, 2234 (2023).
[47] A. Haji-Akbari and P. G. Debenedetti, Direct calculation of ice homogeneous nucleation rate for a molecular model of water, Proc. Natl. Acad. Sci. USA **112**, 10582 (2015).
[48] While this seems obvious for models of different real-life polymer chemistries such as polyethylene and polypropylene, this concept also applies to numerical models of the same physical system with different potentials or parameters.
[49] P.-G. De Gennes, *Scaling Concepts in Polymer Physics* (Cornell University Press, Ithaca, NY, 1979).
[50] W. Paul, D. Y. Yoon, and G. D. Smith, An optimized united atom model for simulations of polymethylene melts, J. Chem. Phys. **103**, 1702 (1995).
[51] W. L. Jorgensen and J. Tirado-Rives, The OPLS [optimized potentials for liquid simulations] potential functions for proteins, energy minimizations for crystals of cyclic peptides and crambin, J. Am. Chem. Soc. **110**, 1657 (1988).
[52] W. L. Jorgensen, D. S. Maxwell, and J. Tirado-Rives, Development and testing of the OPLS all-atom force field on conformational energetics and properties of organic liquids, J. Am. Chem. Soc. **118**, 11225 (1996).
[53] D. Tobias, K. Tu, and M. Klein, Assessment of all-atom potentials for modeling membranes: Molecular dynamics simulations of solid and liquid alkanes and crystals of phospholipid fragments, J. Chim. Phys. **94**, 1482 (1997).
[54] W. Shinoda, R. Devane, and M. L. Klein, Multi-property fitting and parameterization of a coarse grained model for aqueous surfactants, Mol. Simul. **33**, 27 (2007).

[55] K. W. Hall, T. W. Sirk, M. L. Klein, and W. Shinoda, A coarse-grain model for entangled polyethylene melts and polyethylene crystallization, J. Chem. Phys. **150**, 244901 (2019).

[56] M. G. Martin and J. I. Siepmann, Transferable potentials for phase equilibria. 1. United-atom description of *n*-alkanes, J. Phys. Chem. B **102**, 2569 (1998).

[57] J. I. Siepmann, S. Karaborni, and B. Smit, Simulating the critical behaviour of complex fluids, Nature (London) **365**, 330 (1993).

[58] T. T. Foley, M. S. Shell, and W. G. Noid, The impact of resolution upon entropy and information in coarse-grained models, J. Chem. Phys. **143**, 243104 (2015).

[59] T. Shakirov and W. Paul, Crystallization in melts of short, semiflexible hard polymer chains: An interplay of entropies and dimensions, Phys. Rev. E **97**, 042501 (2018).

[60] T. Shakirov, Crystallisation in melts of short, semi-flexible hard-sphere polymer chains: The role of the non-bonded interaction range, Entropy **21**, 856 (2019).

[61] N. C. Karayiannis, K. Foteinopoulou, and M. Laso, Entropy-driven crystallization in dense systems of athermal chain molecules, Phys. Rev. Lett. **103**, 045703 (2009).

[62] H. T. Nguyen, T. B. Smith, R. S. Hoy, and N. C. Karayiannis, Effect of chain stiffness on the competition between crystallization and glass-formation in model unentangled polymers, J. Chem. Phys. **143**, 144901 (2015).

[63] H. T. Nguyen and R. S. Hoy, Effect of chain stiffness and temperature on the dynamics and microstructure of crystallizable bead-spring polymer melts, Phys. Rev. E **94**, 052502 (2016).

[64] R. S. Hoy and N. C. Karayiannis, Simple model for chain packing and crystallization of soft colloidal polymers, Phys. Rev. E **88**, 012601 (2013).

[65] P. J. Steinhardt, D. R. Nelson, and M. Ronchetti, Bond-orientational order in liquids and glasses, Phys. Rev. B **28**, 784 (1983).

[66] A. Reinhardt, J. P. K. K. Doye, E. G. Noya, and C. Vega, Local order parameters for use in driving homogeneous ice nucleation with all-atom models of water, J. Chem. Phys. **137**, 194504 (2012).

[67] P. Kawak, Simulation of crystal nucleation in polymer melts, Ph.D. thesis, Brigham Young University, 2022.

[68] D. R. Tree, A. Muralidhar, P. S. Doyle, and K. D. Dorfman, Is DNA a good model polymer? Macromolecules **46**, 8369 (2013).

[69] T. Shakirov and W. Paul, Folded alkane chains and the emergence of the lamellar crystal, J. Chem. Phys. **150**, 084903 (2019).

[70] See Supplemental Material at http://link.aps.org/supplemental/10.1103/PhysRevMaterials.8.075606 for details on: the parameterization of the various polymer models used in the main text, details related to the effect hard sphere bead size, details related to the calculation of the persistence length, details related to the implementation of the Wang Landau Monte Carlo simulation method including the multi-walker scheme, a complete set of thermal profiles for Model A including a finite-size analysis, a complete set of thermal profiles for Model B, A complete set of thermal profiles for Model C, and details related to the effect of excluded volume on crystallization phase behavior.

[71] H. C. Andersen, J. D. Weeks, and D. Chandler, Relationship between the hard-sphere fluid and fluids with realistic repulsive forces, Phys. Rev. A **4**, 1597 (1971).

[72] F. T. Wall and F. Mandel, Macromolecular dimensions obtained by an efficient Monte Carlo method without sample attrition, J. Chem. Phys. **63**, 4592 (1975).

[73] S. K. Kumar, M. Vacatello, and D. Y. Yoon, Off-lattice Monte Carlo simulations of polymer melts confined between two plates, J. Chem. Phys. **89**, 5206 (1988).

[74] J. J. de Pablo, M. Laso, J. I. Siepmann, and U. W. Suter, Continuum-configurational-bias Monte Carlo simulations of long-chain alkanes, Mol. Phys. **80**, 55 (1993).

[75] J. J. de Pablo, M. Laso, U. W. Suter, and H. D. Cochran, Continuum configurational bias Monte-Carlo studies of alkanes and polyethylene, Fluid Phase Equilib. **83**, 323 (1993).

[76] X.-J. Li and Y. C. Chiew, Monte Carlo simulation of Lennard-Jones chains, J. Chem. Phys. **101**, 2522 (1994).

[77] F. A. Escobedo and J. J. de Pablo, Extended continuum configurational bias Monte Carlo methods for simulation of flexible molecules, J. Chem. Phys. **102**, 2636 (1995).

[78] P. V. K. Pant and D. N. Theodorou, Variable connectivity method for the atomistic Monte Carlo simulation of polydisperse polymer melts, Macromolecules **28**, 7224 (1995).

[79] V. G. Mavrantzas, T. D. Boone, E. Zervopoulou, and D. N. Theodorou, End-bridging Monte Carlo: A fast algorithm for atomistic simulation of condensed phases of long polymer chains, Macromolecules **32**, 5072 (1999).

[80] A. Uhlherr, V. G. Mavrantzas, M. Doxastakis, and D. N. Theodorou, Directed bridging methods for fast atomistic Monte Carlo simulations of bulk polymers, Macromolecules **34**, 8554 (2001).

[81] M. Rubinstein and R. Colby, *Polymer Physics* (Oxford University Press, Oxford, 2003).

[82] M. O. Khan, G. Kennedy, and D. Y. C. Chan, A scalable parallel monte carlo method for free energy simulations of molecular systems, J. Comput. Chem. **26**, 72 (2005).

[83] O. Alexiadis, V. G. Mavrantzas, R. Khare, J. Beckers, and A. R. C. Baljon, End-bridging Monte Carlo simulation of bulk and grafted amorphous polyethylene above and below the glass transition, Macromolecules **41**, 987 (2008).

[84] K. A. Maerzke, L. Gai, P. T. Cummings, and C. McCabe, Incorporating configurational-bias Monte Carlo into the Wang-Landau algorithm for continuous molecular systems, J. Chem. Phys. **137**, 204105 (2012).

[85] T. Vogel, Y. W. Li, T. Wüst, and D. P. Landau, Generic, hierarchical framework for massively parallel Wang-Landau sampling, Phys. Rev. Lett. **110**, 210603 (2013).

[86] Y. W. Li, T. Vogel, T. Wüst, and D. P. Landau, A new paradigm for petascale Monte Carlo simulation: Replica exchange Wang-Landau sampling, J. Phys.: Conf. Ser. **510**, 012012 (2014).

[87] M. E. Mackura and D. S. Simmons, Enhancing heterogenous crystallization resistance in a bead-spring polymer model by modifying bond length, J. Polym. Sci. B Polym. Phys. **52**, 134 (2014).

[88] G. Shi, T. Vogel, T. Wüst, Y. W. Li, and D. P. Landau, Effect of single-site mutations on hydrophobic-polar lattice proteins, Phys. Rev. E **90**, 033307 (2014).

[89] T. Vogel, Y. W. Li, T. Wüst, and D. P. Landau, Scalable replica-exchange framework for Wang-Landau sampling, Phys. Rev. E **90**, 023302 (2014).

[90] T. Hayashi and Y. Okamoto, Efficient simulation protocol for determining the density of states: Combination of

replica-exchange Wang-Landau method and multicanonical replica-exchange method, Phys. Rev. E **100**, 043304 (2019).

[91] S. Torquato, T. M. Truskett, and P. G. Debenedetti, Is random close packing of spheres well defined? Phys. Rev. Lett. **84**, 2064 (2000).

[92] P. M. Ramos, M. Herranz, D. Martínez-Fernández, K. Foteinopoulou, M. Laso, and N. C. Karayiannis, Crystallization of flexible chains of tangent hard spheres under full confinement, J. Phys. Chem. B **126**, 5931 (2022).

[93] D. M. Heyes and H. Okumura, Equation of state and structural properties of the Weeks-Chandler-Andersen fluid, J. Chem. Phys. **124**, 164507 (2006).

[94] A. Ahmed and R. J. Sadus, Phase diagram of the Weeks-Chandler-Andersen potential from very low to high temperatures and pressures, Phys. Rev. E **80**, 061101 (2009).

[95] K. Binder, Finite size effects at phase transitions, in *Computational Methods in Field Theory*, Vol. 409 (Springer, Berlin, 1992), pp. 59–125.

[96] J. Wedekind, D. Reguera, and R. Strey, Finite-size effects in simulations of nucleation, J. Chem. Phys. **125**, 214505 (2006).

[97] S. Sinha and S. K. Roy, Finite size scaling and first-order phase transition in a modified *xy* model, Phys. Rev. E **81**, 022102 (2010).

[98] S. Yuan, Z. Li, Y. L. Hong, Y. Ke, J. Kang, A. Kamimura, A. Otsubo, and T. Miyoshi, Folding of polymer chains in the early stage of crystallization, ACS Macro Lett. **4**, 1382 (2015).